

Image reconstruction for lung monitoring in wearable electrical impedance tomography

Streszczenie. *This work presents a method for measuring and reconstructing human lungs using a waistcoat with an integrated impedance tomograph. The reconstructions obtained make it possible to follow the patient's breathing and, in the case of a 3D model, to determine whether there is fluid in the patient's lungs. The numerical model involves minimising the functional, determining the simulation and the form of the sensitivity matrix. In order to perform the tests, a portable impedance tomography system for biomedical applications was constructed, consisting of a measuring belt and a portable device made of flexible material with 32 round electrodes installed. This solution allows imaging of lung lesions by defining a model and solving the inverse problem using the finite element method.*

Abstract. *Praca przedstawia metodę pomiaru i rekonstrukcji ludzkich płuc przy użyciu kamizelki z wbudowanym tomografem impedancyjnym. Uzyskane rekonstrukcje pozwalają na śledzenie oddychania pacjenta a w przypadku 3D model pozwala stwierdzić czy w płucach pacjenta znajduje się płyn. Model numeryczny polega na minimalizacji funkcjonału, wyznaczaniu symulacji i postaci macierzy wrażliwości. W celu wykonania badań skonstruowano przenośny system tomografii impedancyjnej do zastosowań biomedycznych składający się z pasa pomiarowego oraz przenośnego urządzenia wykonane z elastycznego materiału z zainstalowanymi 32 okrągłymi elektrodami. Takie rozwiązanie umożliwia obrazowanie zmian w płucach poprzez zdefiniowanie modelu i rozwiązując problem odwrotny z wykorzystaniem metody elementów skończonych. (Rekonstrukcja obrazu do monitorowania płuc w przenośnej tomografii impedancyjnej).*

Keywords: elektryczna tomografia impedancyjna, problem odwrotny, obrazowanie medyczne

Słowa kluczowe: rekonstrukcje dla EIT, obrazowanie medyczne

Introduction

Respiratory diseases are among the most significant medical challenges of the modern world. Air pollution, especially emerging in developing countries, health problems affect both the circulatory and respiratory systems. The bad air quality contributes to thousands of excess deaths, which could have been avoided [1]. The recent COVID-19 pandemic also brought significant lung-related complications. The scale of these complications is currently discussed, yet it remains clear that even patients who went through only mild symptoms of infection might suffer from severe lung damage [2]. The long term effects of the massive scale of infections during the pandemic can leave imprints on public health and will set the direction of the progress in medical sciences over the next decade.

From this perspective, it seems that developing cheap, easily accessible and reliable lung monitoring methods is urgently necessary. Electric Impedance Tomography (EIT) meets all of the requirements above. However, achieving the final goal, especially real-time monitoring, is very complex [3-7]. Thus, while the device's construction is relatively simple, the fineness of the technique is contained in the algorithms. Knowing the characteristics of each tomographic technique solution, the application allows the selection of a suitable image reconstruction method [8-14]. Different methods can be used to solve the optimisation process [15-18].

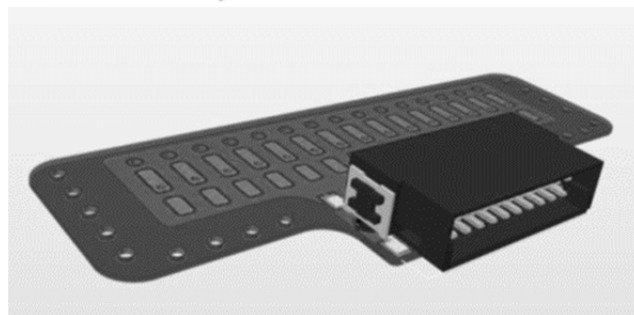
The organisation of the paper is following. First, in Section 2. we discuss the construction of the device. Then, in Section 3. the numerical model used for reconstruction is presented. Next, section 4. contains relevant results from the reconstruction. Finally, in Section 5. we shortly conclude the paper.

Impedance tomograph

The wearable device is based on its predecessor, smartEIT developed and constructed by Netrix. The chest belt is made of the elastic material with 32 round electrodes installed. The device is in the final stage of development.

Some relevant technical parameters are as following:

- power supply voltage: 5 - 16V,
- max. driving frequency: 150kHz,
- TLV5619 and MCP4901 DACs,
- ADG731 - a 32 channel analog multiplexer with resistance 4Ω,
- LTC2202 converters for signal measurements with 16-bit resolution and 10Msps sampling rate,
- evaluation circuit.



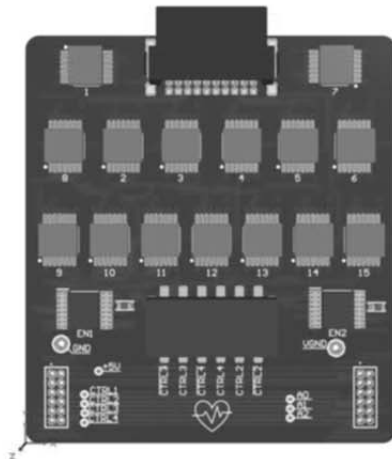
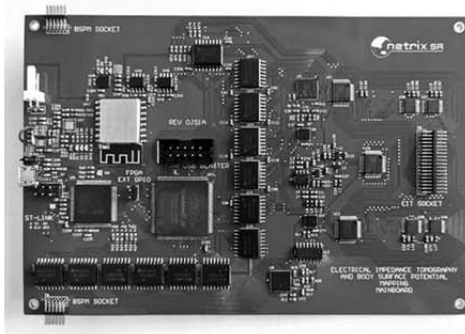
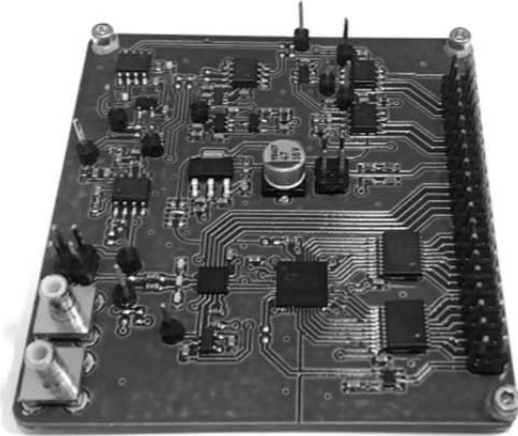
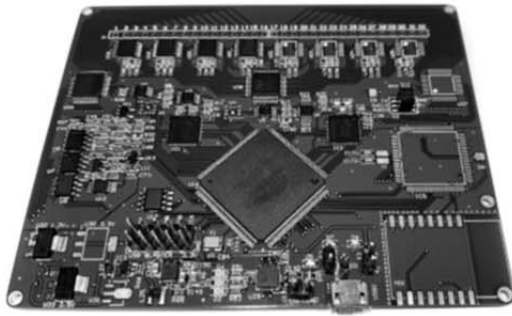


Fig. 1 The pictures of the device circuit boards

Figure 1 presents the circuit board, where some of the mentioned electronic elements are visible.

The system's operation consists of the simultaneous measurement of current and voltage in the EIT mode and the measurement of potentials in the BSPM mode. The data processed by the FPGA and transferred to the microcontroller will then be sent to an external resource.

Therefore, the use of a circuit architecture in which FPGA is responsible for a series of parallel measurements and a microcontroller for communication interfaces is advantageous due to the high speed of such a solution.

Due to the characteristics of impedance tomography measurements and the limited target size of the device (and therefore a limited number of ADCs and power supply from only one initial voltage level), the measurement signals must be multiplexed. It introduces a series of delays that can be partially mitigated by parallel high-frequency processing in the FPGAs. The microcontroller then maps a fragment of the structure of this chip as external RAM. Data is downloaded to the STM32 via the Quad-SPI interface. Then, appropriately formatted, they are forwarded.

Numerical model

Our numerical scheme relies on the minimisation of the functional

$$(1) \quad E(\phi) = \int \int_{\Pi} \|\nabla \phi(v)\|^2 dv + \sum_{z_l} \frac{1}{z_l} \int \int_{\Omega} (\phi - U_l)^2 d\omega$$

with a precondition for minimisation - the zeroing of variance

$$(2) \quad \delta E(\phi) = 2 \int_{\Pi} \sigma \nabla \phi(v) \cdot \nabla (\delta \phi(v)) dv + \sum_{z_l} \frac{2}{z_l} \int_{\Omega} (\phi(v) - U_l) \delta \phi(v) d\omega = 0$$

where ϕ - electric potential, σ - electrical conductivity, U_l - electric potential at electrodes, π - the volume of reconstruction, Ω - the surface of the electrode. We consider tetrahedron elements. For each element, let us assume the interpolating function for the potential is a first-order polynomial

$$(3) \quad \phi(x, y, z) = a + bx + cy + dz$$

In the next step, we perform two transformations to standardize the integration limits for all elements. First, a tetrahedral element is then converted to a unit tetrahedron, using the following formulas

$$(4) \quad \begin{aligned} x &= \sum_m N_m(\xi, \eta, \zeta) x_m \\ y &= \sum_m N_m(\xi, \eta, \zeta) y_m \\ z &= \sum_m N_m(\xi, \eta, \zeta) z_m \end{aligned}$$

where

$$(5) \quad \begin{aligned} N_1(\xi, \eta, \zeta) &= \xi \\ N_2(\xi, \eta, \zeta) &= \eta \\ N_3(\xi, \eta, \zeta) &= \zeta \\ N_4(\xi, \eta, \zeta) &= 1 - \xi - \eta - \zeta \end{aligned}$$

The second is to transform the electrode elements with basic functions, namely

$$(6) \quad \begin{aligned} M_1(\xi, \eta) &= \xi \\ M_2(\xi, \eta) &= \eta \\ M_3(\xi, \eta) &= 1 - \xi - \eta \end{aligned}$$

For one element of the tetrahedron with the face belonging to the l -th electrode, the state matrix is given by

$$(7) \quad \begin{bmatrix} \frac{\partial E^e}{\partial \phi_1} \\ \frac{\partial E^e}{\partial \phi_2} \\ \frac{\partial E^e}{\partial \phi_3} \\ \frac{\partial E^e}{\partial \phi_4} \end{bmatrix} = \begin{bmatrix} h_{11}^e & h_{12}^e & h_{13}^e & h_{14}^e \\ h_{21}^e & h_{22}^e & h_{23}^e & h_{24}^e \\ h_{31}^e & h_{32}^e & h_{33}^e & h_{34}^e \\ h_{41}^e & h_{42}^e & h_{43}^e & h_{44}^e \end{bmatrix} \begin{bmatrix} \phi_1 \\ \phi_2 \\ \phi_3 \\ \phi_4 \end{bmatrix} + \begin{bmatrix} d_{11} & d_{12} & d_{13} & d_{14} \\ d_{21} & d_{22} & d_{23} & d_{24} \\ d_{31} & d_{32} & d_{33} & d_{34} \\ d_{41} & d_{42} & d_{43} & d_{44} \end{bmatrix} \begin{bmatrix} \phi_1 \\ \phi_2 \\ \phi_3 \\ \phi_4 \end{bmatrix}$$

where d_{ij}, d_i, h_{ij}^e – are integrals of equations (2) appropriately second part, the first part with used interpolation function (5), (6).

Then we expand and sum up the matrices h^e, d^e overall elements and take into account the boundary conditions to obtain the state matrix H , which satisfies the general equation

$$(8) \quad H\Phi = 0$$

0 is a vector with a considered stimulation pattern (in the appropriate index are the value of injection power). The solution of this equation is the potential at nodes. Naturally, the potential is necessary for determining the sensitivity matrix, which is determined by equation

$$(9) \quad J = -\frac{1}{I} \int_{\Omega} \nabla \phi \nabla \Psi d\Omega$$

and after expanding the gradients, we have

$$(10) \quad J = -\frac{1}{I} \int \frac{\partial \phi}{\partial x} \frac{\partial \Psi}{\partial x} + \frac{\partial \phi}{\partial y} \frac{\partial \Psi}{\partial y} + \frac{\partial \phi}{\partial z} \frac{\partial \Psi}{\partial z} dx dy dz$$

Here however we distinguish either potentials. Namely, ϕ is the potential at nodes of stimulating electrodes and ψ is the potential at nodes of measuring electrodes. Just like previously, we use interpolating functions N_i

$$(11) \quad \widehat{\phi}(x, y, z) = \sum_{i \in I} N_i \phi_i$$

Next, we transform the equation from (x, y, z) space to (ξ, η, ζ) space. Using the derivations of composite function $\phi(x(\xi, \eta, \zeta), y(\xi, \eta, \zeta), z(\xi, \eta, \zeta))$ we obtain the sensitivity matrix J . To obtain the conductivity reconstruction, we need to compute the pseudoinverse of the sensitivity matrix

$$(12) \quad H_{mat} = (J^T J \cdot I)^{-1}, \quad R_{mat} = J H_{mat}^{-1} J^T + \lambda I$$

Then

$$(13) \quad \widehat{J}^{-1} = H_{mat}^{-1} J^T R_{mat}^{-1}$$

We use this form of pseudoinverse matrix because our mesh has 161920 elements, which prevents an error of memory in workspace Matlab. Finally, we compute the reconstruction with the equation

$$(14) \quad \widehat{\sigma} = \widehat{J}^{-1} V$$

where λ is the regularisation parameter, and V is the differential measurement.

The grid consists of 161920 elements with 32 round electrodes which can be seen in Figure 2.

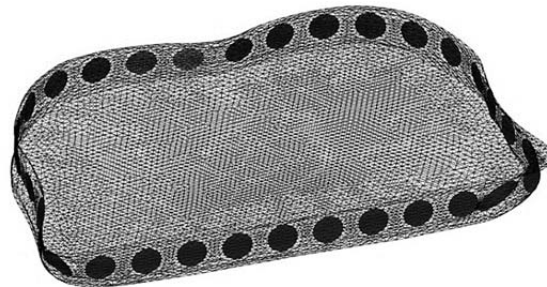


Fig. 2 The computational grid constructed from the CT images.

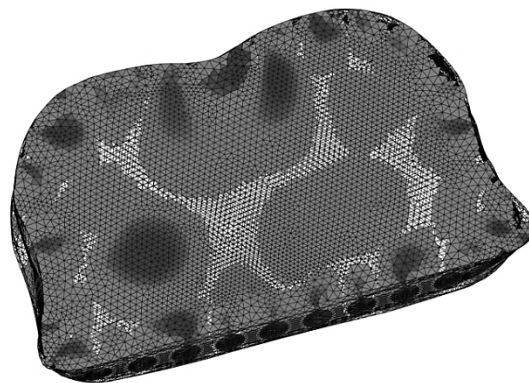


Fig. 3 The reconstructing of the patient's lungs while exhaling the air

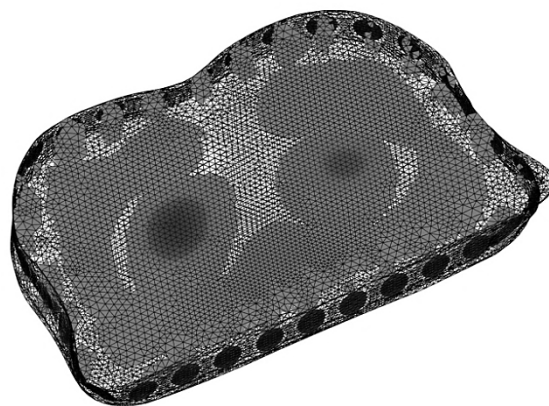


Fig. 4 The reconstructing of the patient's lungs full of air

Results

We made a set of measurements with a current of $3 \mu A$ and an excitation frequency of $150 kHz$. Reconstructions were obtained with regularisation parameter $\lambda = 0.009$ with differential measurement where reference measurement is average of last 100 measurements. The results in Figures 3 and 4 show the reconstructed image for the case of the exhalation and the inhalation, respectively. Two blue regions shown in Figure 4 are the tomographic projection of

the lungs. The blue colour indicates that the conductance of the region is lower than the surrounding area. When the patient exhales, the lungs become more conductive and thus are similar to the surrounding area.

Table 1. Compare of errors in reconstruction on process inhalation and exhalation.

Process	$\ \delta\ $	$\ \delta - V\ $
Inhalation	$6.6365 \cdot 10^{-4}$	$1.5331 \cdot 10^3$
Exhaling	$1.4 \cdot 10^{-3}$	$1.2423 \cdot 10^3$

Figure 5 shows that the average value of the metric measurement is a function of time. Inhalations of the patient correspond with the local minima of the curve - similarly, the exhalations with local maxima. The curve also reveals a descending trend. This is caused by the changing skin conductance, which unfortunately is unavoidable due to the patient sweating.

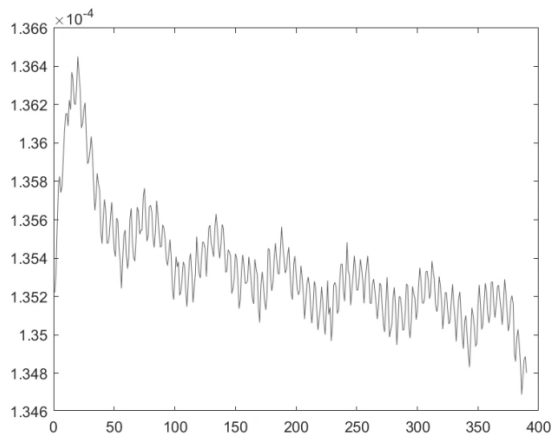


Fig. 5 The average value of the reconstructed measurements as a function following time steps measured in sample numbers.

Summary

In this short paper, we reported the recent development of the wearable EIT based lung monitoring device. The obtained results look promising, especially in broader production and possible application of the device. The 3D reconstruction can also show the patient's regions with some fluid in one's lungs. The regions containing the fluid are much more conductive for the remaining part of the lungs. However, the results still reveal some shortcomings, and some additional post-processing for image improvement is necessary. We shall return to these problems elsewhere.

Authors: dr inż. Dariusz Wójcik Research and Development Center, Netrix S.A., 20-704 Związkowa st. 26, Lublin, Poland E-mail: dariusz.wojcik@netrix.com.pl, prof. dr hab. inż. Tomasz Rymarczyk, Research and Development Center, Netrix S.A., 20-704 Związkowa st. 26, Lublin, Poland, University of Economics and Innovation in Lublin, ul. Projektowa 4, 20-209 Lublin, Poland, E-mail: tomasz.rymarczyk@netrix.com.pl; mgr Barbara Stefaniak Research and Development Center, Netrix S.A., 20-704 Związkowa st. 26, Lublin, Poland, E-mail: barbara.stefaniak@netrix.com.pl, mgr Michał Woś Research and Development Center, Netrix S.A., 20-704 Związkowa st. 26, Lublin, Poland, E-mail: michal.wos@netrix.com.pl, mgr Bartłomiej Kiczek Research and Development Center, Netrix S.A., 20-704 Związkowa st. 26, Lublin, Poland, E-mail: bartlomiej.kiczek@netrix.com.pl.

REFERENCES

- [1] Xiao-Dong Mei Xu-Qin Jiang, Feng D.. 2016. Air pollution and chronic airwaydiseases: what should people know and do? *Journal of Thoracic Disease* (2016), 31–40
- [2] Fraser E. 2020. Long term respiratory complications of COVID-19. *The British Medical Journal*, 370 (Aug. 2020), 3001. <https://doi.org/10.1136/bmj.m3001>
- [3] Rymarczyk T., Bożek P., Oleszek M., Niderla K., and Adamkiewicz A. Construction of the SmartEIT tomograph based on electrical impedance tomography, *Przegląd Elektrotechniczny*, 96 (2020), No. 2, 44–47
- [4] Rymarczyk T., Kosior A., Tchórzewski P., and Vejar A.. Image reconstruction in electrical impedance tomography using a reconfigurable FPGA system. *Journal of Physics: Conference Series*, (2021), 1782, 1, 012033
- [5] Rymarczyk T., Kozłowski E., Tchórzewski P., Kłosowski G., and Adamkiewicz P. Applying the logistic regression in electrical impedance tomography to analyze conductivity of the examined objects. *International Journal of Applied Electromagnetics and Mechanics*, 64 (2020), 235–252
- [6] Rymarczyk T., Kozłowski E., Kłosowski G. Object Analysis Using Machine Learning to Solve Inverse Problem in Electrical Impedance Tomography. *IEEE International Conference on Imaging Systems and Techniques IST* (2018), 1–6
- [7] Rymarczyk T., Kozłowski E., Kłosowski G., Electrical impedance tomography in 3D flood embankments testing – elastic net approach, *Transactions of the Institute of Measurement and Control*, 42 (2020), No. 4, 680-690
- [8] Rymarczyk T., Polakowski K. and Sikora J., PDE-solved by boundary element method for electrical impedance tomography, *Journal of Physics: Conference Series* (2021), 1782 012030
- [9] Rymarczyk T., Characterization of the shape of unknown objects by inverse numerical methods, *Przegląd Elektrotechniczny*, 88 (2012), No.7B, 138-140
- [10] Rymarczyk T, Using electrical impedance tomography to monitoring flood banks 16th International Symposium on Applied Electromagnetics and Mechanics (ISEM), *International journal of applied electromagnetics and mechanics*, 45 (2014), 489-494
- [11] Filipowicz SF, Rymarczyk T., The Shape Reconstruction of Unknown Objects for Inverse Problems, *Przegląd Elektrotechniczny*, 88 (2012), No.3A, 55-57
- [12] Koulountzios P., Rymarczyk T., Soleimani M., A quantitative ultrasonic travel-time tomography system for investigation of liquid compounds elaborations in industrial processes, *Sensors*, 19 (2019), No. 23, 5117
- [13] Kłosowski G., Rymarczyk T., Kania K., Świć A., Cieplak T., Maintenance of industrial reactors based on deep learning driven ultrasound tomography, *Eksploracja i Niezawodność – Maintenance and Reliability*, 22 (2020), No.1, 138–147
- [14] Kłosowski G., Rymarczyk T., Cieplak T., Niderla K., Skowron Ł., Quality Assessment of the Neural Algorithms on the Example of EIT-UST Hybrid Tomography, *Sensors*, 20 (2020), No.11, 3324
- [15] Łukiański M., Wajman R., The diagnostic of two-phase separation process using digital image segmentation algorithms, *Informatyka, Automatyka, Pomiary W Gospodarce I Ochronie Środowiska*, 10 (2020), No.3, 5-8
- [16] Duraj A., Korzeniewska E., Krawczyk A., Classification algorithms to identify changes in resistance. *Przegląd Elektrotechniczny*, 91 (2015), No.12, 82–84
- [17] Krawczyk A.; Korzeniewska E., Magnetophosphenes–history and contemporary implications. *Przegląd Elektrotechniczny*, 94 (2018), No.1, 61–64
- [18] Mosorov V. Rybak G. Sankowski D., Plug Regime Flow Velocity Measurement Problem Based on Correlability Notion and Twin Plane Electrical Capacitance Tomography: Use Case, *Sensors*, 21 (2021), No.6, 2189 DOI: 10.3390/s21062189